

BIOCHEMISTRY

Artificial receptor-mediated phototransduction toward protocellular subcompartmentalization and signaling-encoded logic gates

He Li¹, Yue Yan¹, Jing Chen¹, Ke Shi¹, Chuwen Song¹, Yanglimin Ji^{2,3}, Liyan Jia^{2,3}, Jianming Li⁴, Yan Qiao^{2,3*}, Yiyang Lin^{1*}

Engineering artificial cellular systems capable of perceiving and transmitting external signals across membranes to activate downstream targets and coordinate protocellular responses is key to build cell-cell communications and protolife. Here, we report a synthetic photoreceptor-mediated signaling pathway with the integration of light harvesting, photo-to-chemical energy conversion, signal transmission, and amplification in synthetic cells, which ultimately resulted in protocell subcompartmentalization. Key to our design is a ruthenium-bipyridine complex that acts as a membrane-anchored photoreceptor to convert visible light into chemical information and transduce signals across the lipid membrane via flip-flop motion. By coupling receptor-mediated phototransduction with biological recognition and enzymatic cascade reactions, we further develop protocell signaling-encoded Boolean logic gates. Our results illustrate a minimal cell model to mimic the photoreceptor cells that can transduce the energy of light into intracellular responses and pave the way to modular control over the flow of information for complex metabolic and signaling pathways.

INTRODUCTION

Cellular functions are controlled by a multitude of extracellular signals such as antigens, hormones, neurotransmitters, light, and other chemical or physical cues. The design of artificial cells capable of receiving and transmitting external signals is of significance to the understanding of the complex behaviors of multicellular systems, as well as the construction of cell-cell communications and prototissues (1–9). Recent advances in the development of rudimentary form of cell-like entities (protocells) from self-assembly of lipids (10–18), fatty acids (19, 20), polymers (21–24), inorganic colloidal particles (25), and protein-polymer conjugates (26, 27) have paved the way for the design of coordinated signaling networks involving chemical exchange and information processing within interacting protocell consortia. To address the challenge of protocell signaling, much effort has been devoted to spatial organization of protocells (28–31), arraying of protocell communities (32), incorporation of protein pores (28, 33), light-activated synthetic cells (33–35), and modulating diffusive transport of signaling molecules across the interface (36, 37). In these studies, water-soluble chemical signals such as proton (16), glucose (38), H₂O₂ (39), DNA (40), and RNA (41) were able to diffuse directly through biomimetic membranes to initiate responses.

In biology, cells decipher a diverse array of messages by taking advantage of cell surface receptors such as G protein-coupled receptors (GPCRs) and receptor tyrosine kinases (RTKs) to recognize

regulatory factors (e.g., ligands and physical cues) and elicit the precise signaling cascade, information processing, and cellular responses (42). Receptor-mediated signal transduction does not require the passage of water-soluble molecules across hydrophobic lipid bilayers, avoiding the entry of toxic species into cytoplasm. To replicate the specificity of signal recognition and the complexity of information processing pathway mediated by cell surface receptors, it is important to repurpose physical parts and concepts from natural receptors and engineer synthetic counterparts as mimics of GPCRs and RTKs (43–49). An alternative approach to rebuild cellular signaling cascades is to reconstruct natural signaling machineries into the membranes of artificial cells (50).

Inspired by the ubiquitous phototransduction in biology, we sought to develop a class of artificial photoreceptors that were specifically anchored on the outer leaf of phospholipid bilayers through hydrophobic interaction (step 1; Fig. 1A), selectively sensed the light illumination, and rapidly converted the photon signals into chemical information of a messenger (step 2). Subsequently following a flip-flop process (step 3), the messenger translocated to the interior of artificial cells to initiate a catalytic reaction for signal amplification (step 4), which eventually promoted confined liquid-liquid phase separation (LLPS; step 5) in artificial cells. We then evaluated the efficiency of photoreceptor-mediated signal transduction by examining a range of physiochemical factors (e.g., membrane fluidity, molecular structures of photoreceptors, and signaling inhibitors). On the basis of these findings, we further coupled the artificial phototransduction with a variety of extracellular signals (e.g., acidity, sucrose, urea, metal ions, and enzymes) to develop protocell-based Boolean logic gates (Fig. 1A).

¹State Key Laboratory of Chemical Resource Engineering, Beijing Laboratory of Biomedical Materials, Beijing University of Chemical Technology, Beijing 100029, China. ²Beijing National Laboratory for Molecular Sciences (BNLMS), Laboratory of Polymer Physics and Chemistry, CAS Research/Education Center for Excellence in Molecular Sciences, Institute of Chemistry, Chinese Academy of Sciences, Beijing 100190, China. ³University of Chinese Academy of Sciences, Beijing 100049, China. ⁴Research Center of New Energy, Research Institute of Petroleum Exploration and Development (RIPED), PetroChina, Beijing 100083, China.

*Corresponding author. Email: yanqiao@iccas.ac.cn (Y.Q.); y.lin@mail.buct.edu.cn (Y.L.)

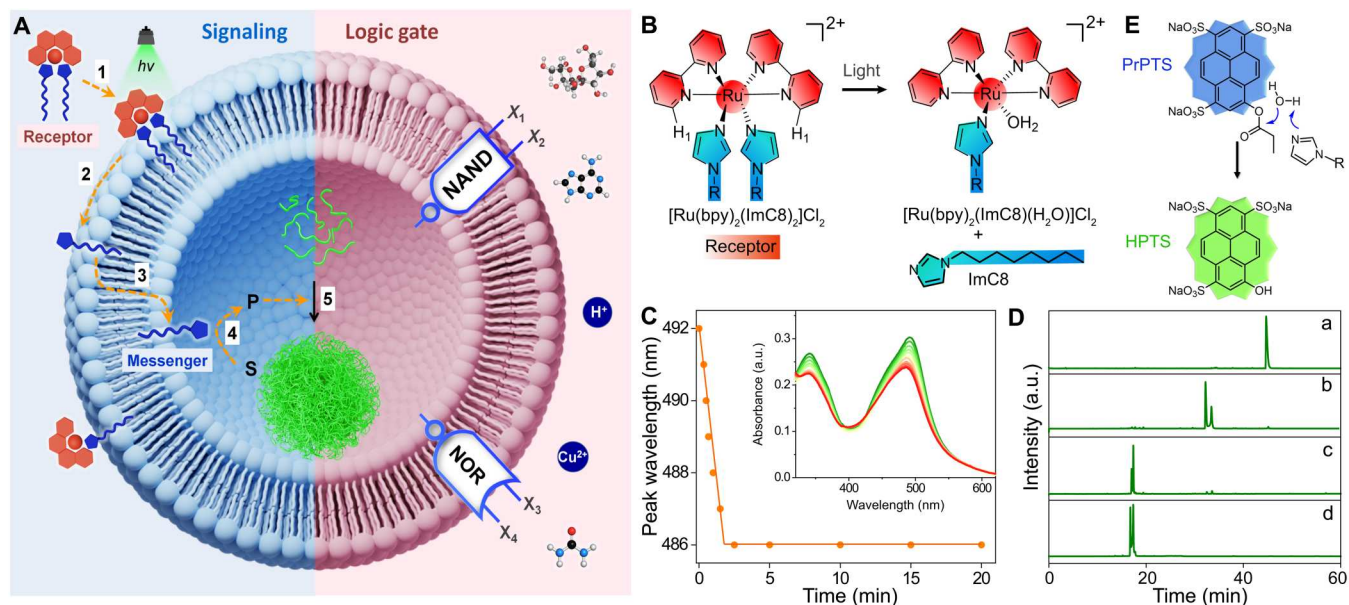


Fig. 1. Synthetic receptor-mediated phototransduction and construction of Boolean logic gates. (A) Left: Phototransduction in artificial cells involving five steps: Spontaneous insertion of a photoreceptor on the lipid membrane (1), photosensitization to excite the receptors and release a messenger (2), the translocation of messenger across the lipid membrane (3), chemical signal amplification through messenger-catalyzed hydrolysis of an esterase substrate (S) to afford a fluorescent product (P) (4), and the formation of coacervate microdroplets (5). Right: Development of Boolean logic gates by coupling photoreceptor-mediated transmembrane signaling with biological recognition and enzymatic cascade reactions, in which extracellular signals (e.g., sucrose and enzyme) were processed as inputs and transmitted into the interior, generating fluorescence amplification and subcompartmentalization as the output signals. (B) Structure of photoreceptor consisting of 1-octylimidazole (ImC8) as the messenger and Ru-bipyridine as the caging and light-harvesting group, which underwent deprotection to liberate one ImC8 upon exposure to light. (C) Activating photoreceptor with 450-nm light caused the decrease of MLCT absorption (inset) and concomitant peak wavelength shifts, confirming the release of ImC8 (messenger) from ruthenium complex. a.u., arbitrary units. (D) HPLC trace of photoreceptor $[\text{Ru}(\text{bpy})_2(\text{ImC8})_2]\text{Cl}_2$ (a), photoactivated product of $[\text{Ru}(\text{bpy})_2(\text{ImC8})_2]\text{Cl}_2$ in water (b) and acetonitrile (c), and $[\text{Ru}(\text{bpy})_2(\text{H}_2\text{O})_2]\text{Cl}_2$ (d), demonstrating the efficient phototriggered degradation of photoreceptor and the liberation of one ImC8 in water. The retention time of photoproduct $[\text{Ru}(\text{bpy})_2(\text{ImC8})(\text{H}_2\text{O})]\text{Cl}_2$ was shorter than $[\text{Ru}(\text{bpy})_2(\text{ImC8})_2]\text{Cl}_2$ but longer than $[\text{Ru}(\text{bpy})_2(\text{H}_2\text{O})_2]\text{Cl}_2$. (E) Schematic of ImC8-catalyzed hydrolysis of nonfluorescent PrPTS into fluorescent 8-hydroxypyrene-1,3,6-trisulfonic acid trisodium (HPTS). The blue arrows indicate a possible general base mechanism.

RESULTS

Design of membrane-anchored photoreceptors

To address the concept described in Fig. 1A, we designed a series of amphiphilic ruthenium complex chromophores $[\text{Ru}(\text{bpy})_2(\text{Im})_2]\text{Cl}_2$ as light-harvesting membrane receptors or photoreceptors (Fig. 1B and fig. S1), which have a ruthenium center (Ru), two bipyridine ligands (bpy), and two alkyl imidazole ligands (Im). Taking $[\text{Ru}(\text{bpy})_2(\text{ImC8})_2]\text{Cl}_2$ as an example, we observed a strong absorption across a large spectral range (300 to 550 nm) with an extinction coefficient (6.2×10^3 liters mol^{-1} cm^{-1} at 492 nm), arising from metal-to-ligand charge transfer (MLCT). Upon illuminated with 450-nm light, we noticed spectral blue shifts and intensity decreases of the MLCT absorption bands (Fig. 1C), suggesting the release of 1-octylimidazole (ImC8) as a messenger in phototransduction. Fluorescence and nuclear magnetic resonance (NMR) spectroscopy (figs. S2 and S3) also confirmed the photocleavage of coordination bond (51). In this reaction, we proposed that $[\text{Ru}(\text{bpy})_2(\text{ImC8})_2]\text{Cl}_2$ underwent ligand dissociation that involved the transition between the MLCT states to a lower-energy *d-d* state, followed by coordination of a water molecule to generate $[\text{Ru}(\text{bpy})_2(\text{ImC8})(\text{H}_2\text{O})]\text{Cl}_2$ (Fig. 1B). Despite the possibility of releasing two ImC8 ligands in water/acetonitrile solution (fig. S4), photoactivation of $[\text{Ru}(\text{bpy})_2(\text{ImC8})_2]\text{Cl}_2$ in aqueous solution liberated only one

ImC8, as proven by high-performance liquid chromatography (HPLC; Fig. 1D).

Imidazole is the main moiety in histidine that is ubiquitous in the active sites of enzymes (e.g., esterase) to perform either nucleophilic or acid/base catalysis. Here, alkyl imidazole fulfills the basic requirements to function as an artificial enzyme (minimal) for signal amplification. By using 1-propyl pyrene-3,6,8-trisulfonate (PrPTS) as a fluorogenic substrate and *p*-nitrophenyl acetate (pNPA) as a chromogenic substrate (Fig. 1E and figs. S5 to S7), we confirmed the catalytic activity of ImC8. Photoactivation of $[\text{Ru}(\text{bpy})_2(\text{ImC8})_2]\text{Cl}_2$ generated a catalytic activity comparable to that of ImC8 (figs. S8 to S10), indicating the stoichiometric release of one catalytically active messenger from one photoreceptor. In addition, our synthetic photoreceptor exhibited wavelength selectivity in activating the esterase-like activity with the visible light of violet, blue, and green colors (400 to 515 nm) but was inert to yellow and red light (figs. S11 and S12).

Photoreceptor-mediated signal transduction

Having established the photosensitization and photoactivation of $[\text{Ru}(\text{bpy})_2(\text{ImC8})_2]\text{Cl}_2$, as well as messenger-triggered signal amplification, we then sought to validate the phototransduction across artificial membranes. To this end, we prepared giant vesicles (GVs) from 1-palmitoyl-2-oleoyl-glycero-3-phosphocholine

(POPC), compartmentalized PrPTS (fluorogenic substrate) within GV, and immobilized $[\text{Ru}(\text{bpy})_2(\text{ImC8})_2]\text{Cl}_2$ (photoreceptor) on the outer leaf of the lipid membrane of GVs. The presence of alkyl chains on the photoreceptor allowed for efficient incorporation (>99%; see Materials and Methods) into the phospholipid membrane spontaneously through hydrophobic interaction.

A key assumption in our experimental design was that photoreceptors located exclusively on the outer leaf of phospholipid bilayers. To prove this, we performed distance-dependent fluorescence resonance energy transfer (FRET) between $[\text{Ru}(\text{bpy})_2(\text{ImC8})_2]\text{Cl}_2$ (acceptor) and 8-hydroxypyrene-1,3,6-trisulfonic acid trisodium (HPTS; donor) (fig. S13). As illustrated in Fig. 2A, the location of photoreceptors on the inner leaf of lipid membrane and the encapsulation of HPTS within GVs will activate FRET; by contrast, the location of photoreceptors on the outer leaf will inhibit FRET, as the presence of lipid bilayer (~6.4-nm thickness for POPC) enlarges

the donor-acceptor distance. In our experiment, direct mixing of $[\text{Ru}(\text{bpy})_2(\text{ImC8})_2]\text{Cl}_2$ and HPTS in solution resulted in a loss of HPTS fluorescence by 60%, indicative of efficient FRET (Fig. 2B). In a solution of photoreceptor-anchored GVs, the quenching effect arising from FRET occurred only when HPTS located outside GVs but was not observed when HPTS was inside GVs (Fig. 2, A and B). We therefore confirmed that photoreceptors preferentially located on the outer leaf and their dislocation across the membrane did not occur because passive diffusion of hydrated metallocomplex across hydrophobic barriers was disfavored.

To build the receptor-mediated phototransduction system, we immobilized photoreceptor on the outer leaf of POPC GVs and encapsulated PrPTS inside GVs (Fig. 2C). Upon illumination with blue light (450 nm), we observed a progressive increase in HPTS fluorescence, indicating the occurrence of signal transduction that elicited the PrPTS-to-HPTS conversion (Fig. 2D and fig. S14). The

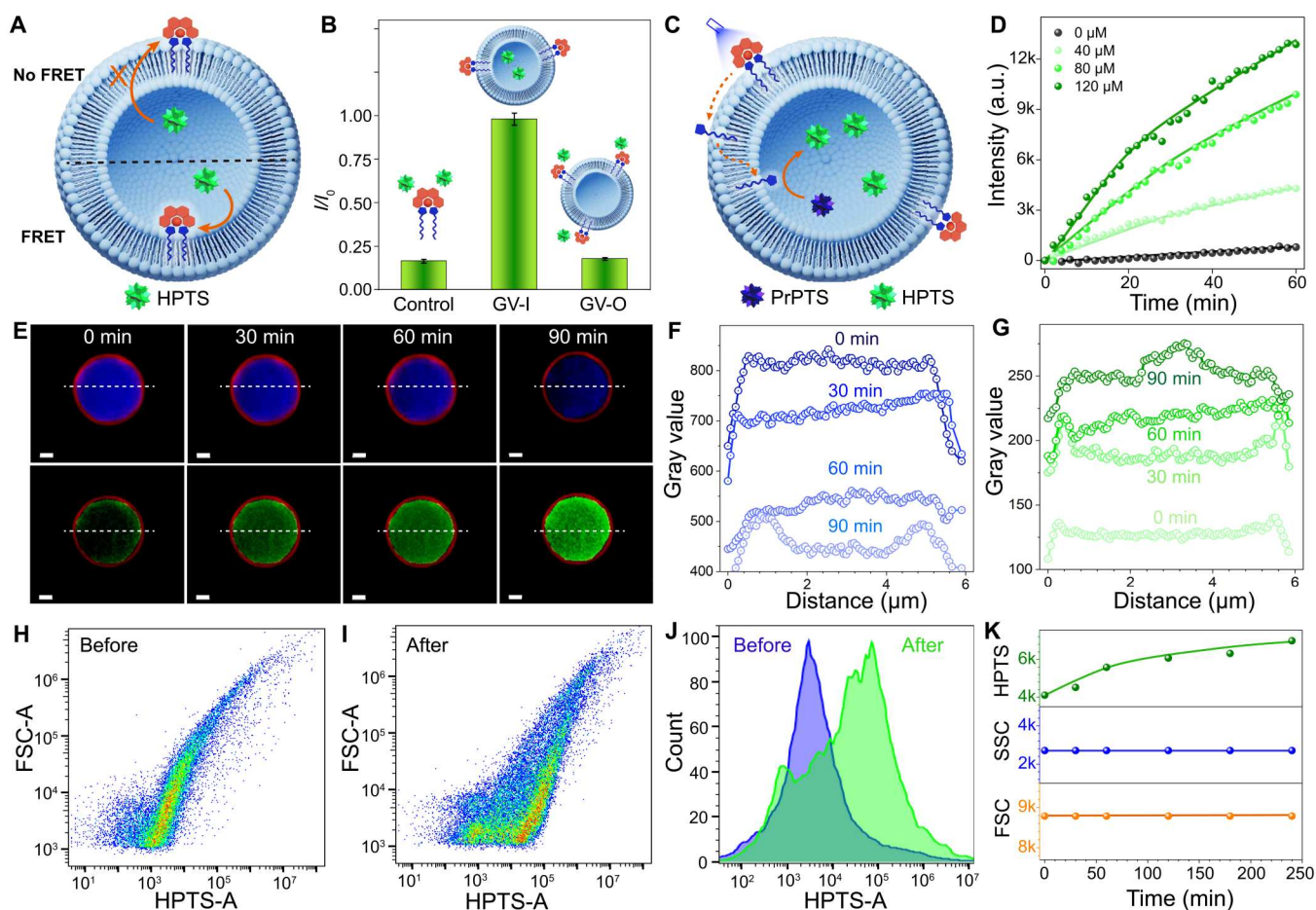


Fig. 2. Phototransduction across artificial membranes. (A) Illustration of two possibilities of photoreceptor distribution on the phospholipid bilayer, in which distance-dependent FRET took place between HPTS (inside GVs) and $[\text{Ru}(\text{bpy})_2(\text{ImC8})_2]\text{Cl}_2$ on the inner leaf. In contrast, FRET was inhibited for photoreceptors located on the outer leaf. (B) Fluorescence quenching (I/I_0) of HPTS by $[\text{Ru}(\text{bpy})_2(\text{ImC8})_2]\text{Cl}_2$. In control solution, electrostatic complexation between HPTS and $[\text{Ru}(\text{bpy})_2(\text{ImC8})_2]\text{Cl}_2$ caused fluorescence quenching via FRET. When photoreceptors were inserted in lipid membrane, FRET occurred only when HPTS located outside vesicles (GV-O) but not in the case that HPTS was encapsulated inside vesicles (GV-I). I and I_0 were fluorescence intensities of HPTS in the presence and absence of photoreceptors, respectively. Error bars represent SD of three replication. (C and D) Photoreceptor-mediated signal transduction: (C) Schematic illustration and (D) fluorescence increase representing signal transduction and amplification after illuminated with 450-nm light. (E to G) Time-lapse fluorescence microscopy images of a POPC GV (stained with Nile red) showing the conversion of PrPTS (blue) into HPTS (green) over time. Profile of line scanning of blue (F) and green fluorescence (G) across the GV in (E) showed an increased level of HPTS and a decreased level of PrPTS, respectively. Scale bars, 1.0 μm . (H to K) Flow cytometry of transmembrane signaling across GVs: (H) Before and (I) after photo-activated signaling. The progressive generation of fluorescent HPTS was confirmed by flow cytometry (H to J), while FSC and SSC remained largely unaffected.

fluorescence enhancement was dependent on the concentration of photoreceptors, where a higher level of photoreceptors boosted the signal transduction. The possibility of PrPTS leakage from GVs that might contribute to the hydrolysis of PrPTS was ruled out (fig. S15). Time-lapse fluorescence microscopy visualization on a single GV showed a loss of blue fluorescence (PrPTS) and a concurrent increase in green fluorescence (HPTS) as a function of incubation time after photostimulation (Fig. 2, E to G), indicative of phototransduction. Flow cytometry collectively quantified the signal transduction, where the HPTS fluorescence continuously increased over a period of 4 hours, while the intensity of front scattering light (FSC) and side scattering light (SSC) remained largely unchanged (Fig. 2, H to K, and fig. S16), suggesting that the size and internal complexity of GVs did not change in the course of phototransduction.

On the basis of the above results, we demonstrated that photoreceptors were capable of sensing the visible light in a color-dependent manner and converting photon energy into a chemical signal by secreting a catalytic messenger (ImC8). Following a flip-flop translocation to the inner lipid membrane leaf, the messenger was able to initiate a catalytic reaction for signal amplification (Fig. 1A).

Physiochemical factors affecting phototransduction

Apparently, a key step for phototransduction was the translocation of messenger across lipid membranes presumably through flip-flop movement, a process of passive diffusion. Hence, membrane organization, environmental temperature, and the structure of messengers were anticipated to affect the efficiency of phototransduction.

We first examined the phototransduction in large unilamellar vesicles (LUVs) with different lipid compositions including 1,2-dipalmitoyl-*sn*-glycero-3-phosphocholine (DPPC; $T_m = 41^\circ\text{C}$), 1,2-dimyristoyl-*sn*-glycero-3-phosphocholine (DMPC; $T_m = 24^\circ\text{C}$), POPC ($T_m = -3^\circ\text{C}$), and POPC/cholesterol (Fig. 3, A to C, and fig. S17). The efficiency of signal transduction as reflected from the fluorescence amplification followed the trend of DPPC < DMPC < POPC/cholesterol < POPC (Fig. 3D). To rationalize this, we used Laurdan as an environment-sensitive probe to detect the membrane phase properties, in which the presence of interfacial water caused shifts in the Laurdan emission spectrum. This allowed us to calculate the generalized polarization (GP) and determine the phospholipid order from changes in membrane fluidity, which was in the order of DPPC > DMPC > POPC/cholesterol > POPC (Fig. 3E), opposite to the rate of signal transduction. We therefore proposed that lower membranous fluidity favored flip-flop translocation of messengers and thereby promoted phototransduction.

Temperature is another biologically relevant factor that governs the fluidity of lipid membranes. We therefore explored the impact of environmental temperature on the receptor-mediated signaling across the lipid membrane of DPPC LUVs. Fluorescence amplification arising from signal transduction was found to increase sharply above a threshold temperature of ca. 41°C , the phase transition temperature (T_m) of DPPC, which was also in accord with the trend of GP (Fig. 3F). We speculated that membrane fluidity of DPPC LUVs became vastly increased above T_m (41°C) as the hydrocarbon chains were randomly oriented into a disordered liquid crystalline phase, which ultimately favored flip-flop translocation of messengers across DPPC membrane. By contrast, the hydrocarbon chains remained fully extended and closely packed (an ordered gel phase)

at temperatures below T_m , in which case molecular diffusion was restricted.

Having established the phototransduction with $[\text{Ru}(\text{bpy})_2(\text{ImC8})_2]\text{Cl}_2$, we then compared the signaling efficiency of a series of synthetic photoreceptors (Rec-1 to Rec-5; Fig. 3G and figs. S18 and S19) to unveil the role of molecular structures. All the receptors have the same headgroup of $\text{Ru}(\text{bpy})_2(\text{Im})_2$, while the hydrophobic tails attached to imidazole were chemically varied. By comparing the results of Rec-1, Rec-2, and Rec-4, we confirmed that photoreceptors with shorter alkyl chain mediated faster phototransduction, in the sequence order of Rec-1 (ImC8) > Rec-2 (ImC10) > Rec-4 (ImC12) (Fig. 3H). Having the same length as Rec-1, Rec-3 with an additional hydroxyl group ($-\text{OH}$) on the hydrocarbon chain displayed an increased molecular polarity and a slow diffusive translocation across apolar membrane. Similarly, Rec-5 with a polar amide bond on the alkyl chain exhibited lower phototransduction efficiency than Rec-2.

Phototransduction-triggered confined LLPS

Having engineering a photoreceptor-mediated transmembrane signaling pathway, we further sought to transduce the photon energy into amplified signal to induce LLPS in artificial cells, a process underlying the formation of membraneless organelles and a series of cellular processes (52).

We first validated the possibility of using amplified chemical signal (HPTS) to trigger LLPS. To test this idea, we examined electrostatic complexation of HPTS with a cationic polyelectrolyte diethylaminoethyl dextran (DEAE-dextran) and observed the phenomenon of complex coacervation driven by multivalent charge attraction (fig. S20). Compared to HPTS that carries four negative charges, PrPTS has only three charges from sulfonate groups, and hence, electrostatic coacervation of PrPTS/DEAE-dextran occurred at a higher level of PrPTS. We therefore anticipated that ImC8 (messenger) can act as an artificial enzyme to catalyze PrPTS-to-HPTS conversion which eventually triggered LLPS in PrPTS/DEAE-dextran solution (fig. S21). Flow cytometry demonstrated the ImC8-catalyzed complex coacervation, in which the scattering of FSC and SSC was progressively intensified as a function of time, indicating the formation of coacervate droplets with high internal complexity (figs. S22 and S23).

To implement phototransduction with confined LLPS in artificial cells, we co-encapsulated DEAE-dextran (polycation) and PrPTS (enzymatic substrate) within POPC GVs and immobilized Rec-1 (photoreceptor) on the outer leaf of lipid membrane (Fig. 4A). Upon irradiation with a 450-nm light, this construct subsequently provoked an instant increase of green fluorescence at 520 nm that resulted from the hydrolysis of PrPTS into HPTS (Fig. 4B). We then used time-lapse fluorescence microscopy to track the changes in GVs, in which blue fluorescence was evenly distributed within GVs before light illumination (Fig. 4C), excluding the possibility of forming DEAE-dextran/PrPTS droplets. Upon photoactivation, coacervate microdroplets as a condensed phase with strong green fluorescence appeared (Fig. 4, D to G). We performed fluorescence recovery after photobleaching (FRAP) experiments using HPTS as a probe to determine the fluidity of coacervate droplets. Photobleaching a small section of the droplet gave rise to a fast recovery (~ 10 s) of fluorescence intensity, suggesting a rapid molecular diffusion and a liquid-phase state inside coacervate microdroplets (fig. S24). Elevating the concentration of DEAE-

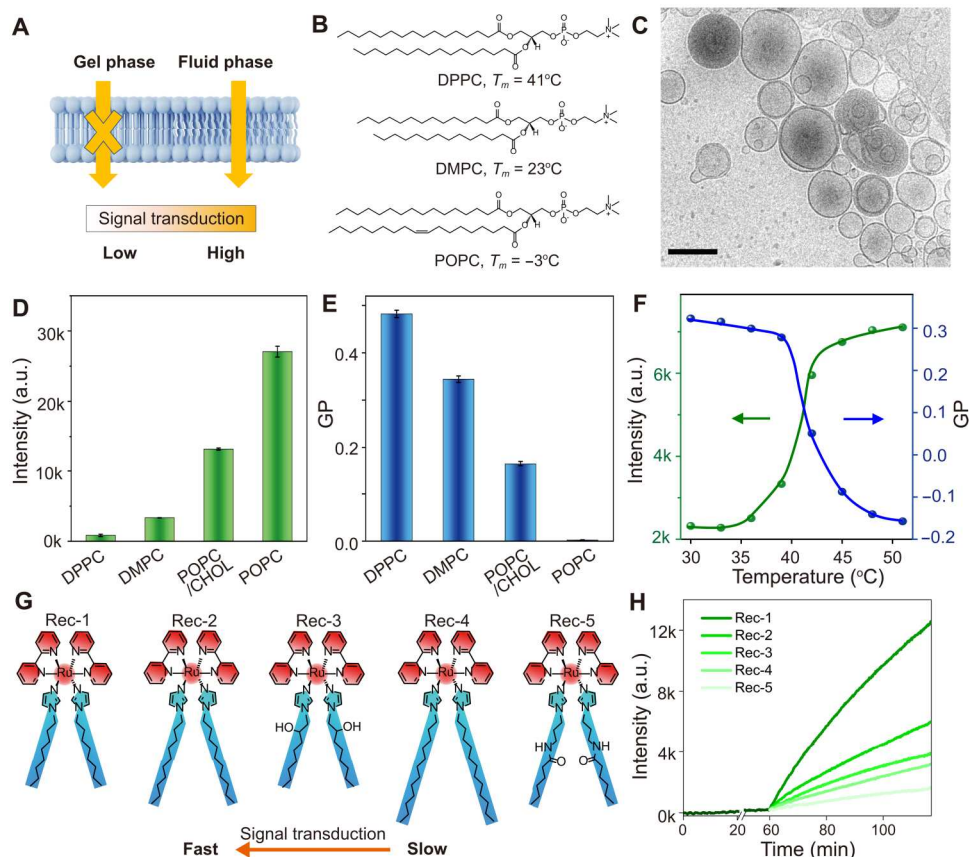


Fig. 3. Parameters influencing photoreceptor-mediated signal transduction. (A) Schematic illustration of membrane fluidity-dependent signaling, in which transmembrane signaling across fluidic phase of lipid membrane was favored. Signal transduction across the lipid membrane was achieved through flip-flop motion of messenger (alkyl imidazole). Hence, an ordered lipid membrane or gel phase suppressed the passive diffusion of messenger and thereby inhibited signal transduction. (B) Lipid structures and corresponding phase transition temperature (T_m) of phospholipid bilayers from DPPC, DMPC, and POPC was 41° , 23° , and -3°C , respectively. (C) A representative cryo-transmission electron microscopy image of POPC LUVs (200 nm). (D) Fluorescence increase arising from phototransduction that led to PrPTS-to-HPTS conversion in LUVs over a period of 60 min. (E) Lipid ordering calculated from Laurdan GP of different lipid composition. (F) Effect of solution temperature on the signal transduction and membrane ordering parameter (i.e., GP) of DPPC LUVs. (G) Molecular structures of photoreceptors exhibiting varied lengths of hydrophobic tails (Rec-1, Rec-2, and Rec-4) or incorporation with a hydroxyl group (Rec-3) or an amide bond (Rec-5). (H) Photoreceptor-mediated signal transduction and amplification in POPC vesicles were manifested by the increase in HPTS fluorescence (520 nm). Error bars represent SD of three replications.

dextran and PrPTS increased the density of coacervates within POPC GV, while the mean diameters of subcompartmentalized microdroplets were smaller (Fig. 4G). This is because, under our experiment condition, phototransduction generated the same amount of HPTS, and hence, higher concentration of polycation resulted in a status far from electrostatic neutralization, which favored the formation of small coacervate microdroplets. We then applied time-dependent flow cytometry to analyze LLPS within GVs (Fig. 4, H to K), which showed a continuous increase in green fluorescence [fluorescein isothiocyanate A (FITC-A)] and SSC from each single GV upon photoactivation. The FSC remained essentially unchanged, suggesting that the confined coacervation increased the internal complexity of artificial cells and the size of GVs stayed constant.

Notably, the coacervate droplets inside GVs were much smaller than those formed in bulk solution, likely because of the confinement effect offered by the lipid membrane, which prevented the recruitment of polycation and HPTS from outside the lipid membrane via passive diffusion of DEAE-dextran and PrPTS (4).

In contrast, coacervation in solution can be fueled by sequestering and condensing polyelectrolytes, resulting in continuous growth of cell-sized droplets via coagulation or Ostwald ripening (53).

Construction of protocell logic gates from transmembrane signaling

Having established a protocell system capable of transducing photon energy into intracellular chemical signal and initiating confined LLPS, we next sought to construct Boolean logic gates by coupling physiochemical changes outside GVs with signal transduction. To achieve this, we incorporated two rudimentary mechanisms for regulating signaling pathways, i.e., metal ions and pH, which enabled us to design logic gates by using external signals as the inputs. We first investigated the role of metal ions, in which coordinating metal ions such as Zn^{2+} , Co^{2+} , Ni^{2+} , Cd^{2+} , and Cu^{2+} prohibited the signal transduction, while Ca^{2+} , Mg^{2+} , and Mn^{2+} did not exhibit inhibitory effect (Fig. 5A and fig. S25). This result was due to the varied stability constant of a metal-imidazole complex for different ions (54): Cu^{2+} ($\log K = 4.23$), Ni^{2+} ($\log K = 3.04$), Co^{2+}

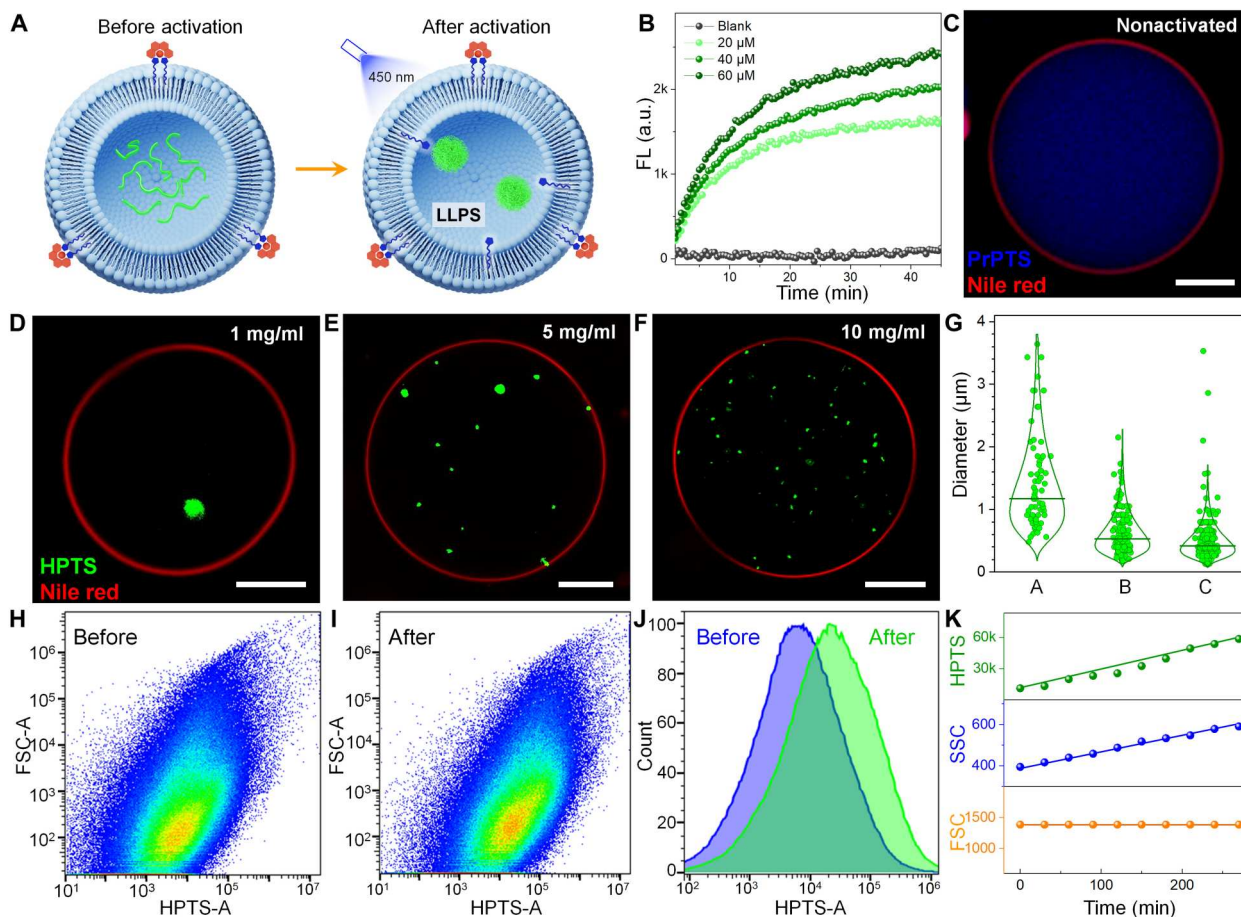


Fig. 4. Phototransduction-mediated confined LLPS. (A) Schematic illustration of photoreceptor-mediated signal transduction across the lipid membrane of GV, which initiated the hydrolysis of PrPTS into HPTS and subsequent electrostatic complexation of DEAE-dextran/PrPTS into coacervate microdroplets via LLPS. (B) Time-dependent fluorescence (FL) intensity and (C to G) fluorescence microscopy images confirming the formation of coacervate microdroplets. (C) Homogeneous distribution of PrPTS was observed in cell-sized POPC GV loaded with DEAE-dextran (1 mg/ml), excluding the possibility of molecular aggregation or particle formation. Upon photoactivation, coacervate microdroplets emitting green fluorescence arising from its hydrolysis product HPTS were observed. Experiments were undertaken at DEAE-dextran concentration of 1.0 (D), 5.0 (E), and 10 mg/ml (F). (G) Box plots of size distribution of coacervate microdroplets inside GV showing the median diameters of 1.4, 0.6, and 0.5 μm for DEAE-dextran levels of 1.0, 5.0, and 10 mg/ml, respectively. Unexpectedly, smaller coacervate microdroplets were formed at elevated concentrations of DEAE-dextran. (H to K) Flow cytometry analysis of signal transduction-mediated confined LLPS within GV. Two-dimensional pseudo-color dot plots of FSC versus FITC fluorescence before (H) and after (I) photoactivation showing the enhancement of FITC fluorescence after photoactivation (J). Meanwhile, SSC progressively increased with a period of 300 min, implying the increased internal complexity arising from complex coacervation. In contrast, the value of FSC remained unchanged, suggesting that the size of GV did not change in the course of transmembrane signaling.

($\log K = 2.46$), Zn^{2+} ($\log K = 2.54$), Cd^{2+} ($\log K = 2.76$), Mn^{2+} ($\log K = 1.38$), Mg^{2+} ($\log K = 0.12$), and Ca^{2+} ($\log K = -0.2$). Presumably, metal-imidazole chelation imparted positive charges to imidazole, enlarged its hydration radius, and lowered the propensity of passive diffusion of ImC8 across the lipid membrane. This restricted the flip-flop translocation of ImC8 across the protocell membrane and blocked the signaling pathway. In particular, metal ions with a stronger binding affinity (e.g., copper ion) exerted higher inhibitory effect.

Imidazole is known to a pH-sensitive moiety at physiologically relevant pHs [$\text{p}K_{\text{a}} = 7.2$ (where K_{a} is the acid dissociation constant); fig. S26], which undergoes protonation under acidic conditions and deprotonation under basic conditions. We then evaluated the impact of environmental pH on signal transduction across the protocell membrane and observed suppressed photo-to-chemical

signal transduction as the solution pH decreased from 8.0 to 6.0 (fig. S27), which was ascribed to imidazole protonation that inhibited the flip-flop motion of ImC8.

The vesicle signaling system in combination with additional chemical components can generate NOR and NAND logic. To design a NOR logic gate (Fig. 5, B and C), we exposed our phototransduction system (photoreceptor on the outer membrane and PrPTS in the internal cavity) to aqueous environments containing copper ions (input A) or acid (pH 6, input B), where the presence of either inputs resulted in the inhibition of flip-flop movement of the messenger and the blockage of transmembrane signaling (0 for output). It was only when copper ion and acid were both absent in solution [viz., (0,0) for input] that signal transduction became valid (1 for output) and LLPS within protocellular microcompartments occurred (Fig. 5D).

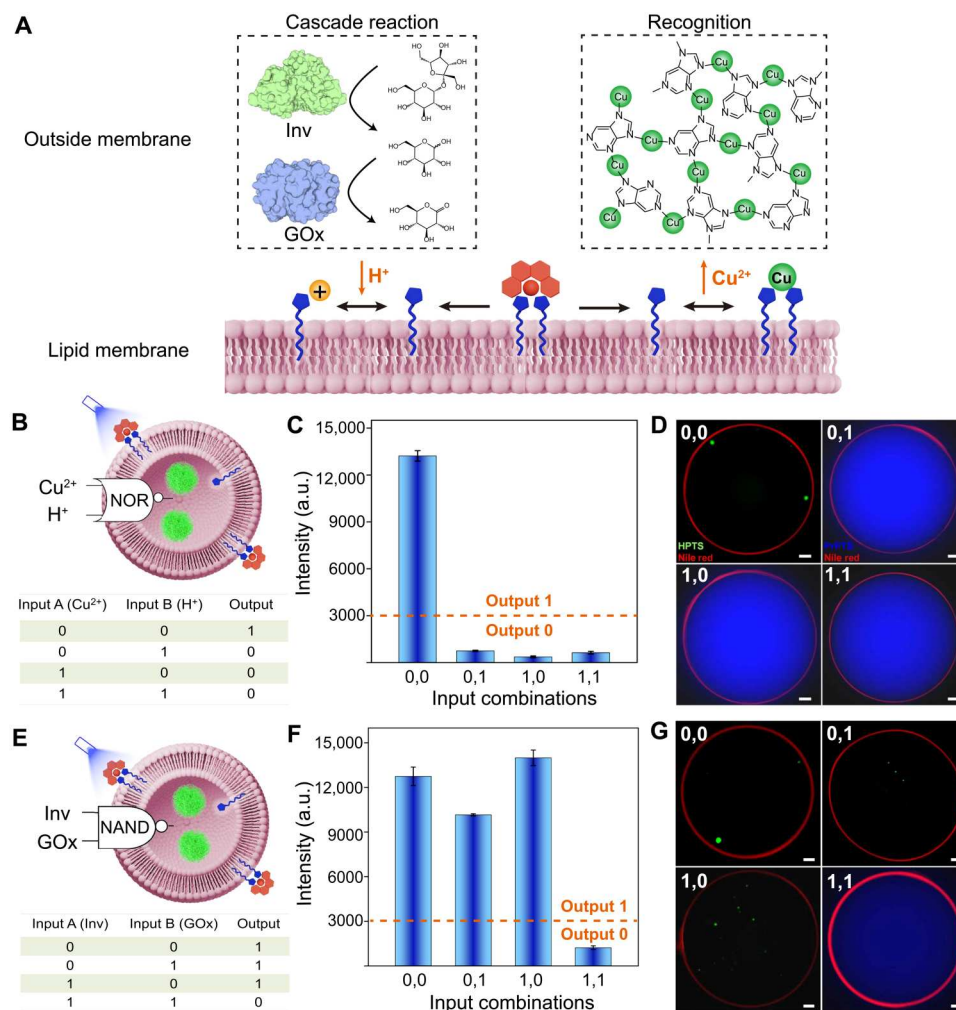


Fig. 5. Construction of Boolean logic gates. (A) Schematic showing metal-ligand recognition and cascade enzymatic reactions that can regulate transmembrane signaling by modulating copper-imidazole chelation and imidazole protonation at the membrane surface. (B to D) Construction of NOR gates: (B) Truth table, (C) fluorescence outputs, and (D) fluorescence microscopy images. Phototransduction system was interfaced with copper ions (1.0 mM, input A) and acid (pH 6, input B), where signaling became possible (1 for output) only when copper ion and acid were both absent [i.e., (0,0) for input]. In contrast, the presence of either input resulted in the inhibition of phototransduction. Signal transduction was observed from the formation of coacervates. Scale bars, 7 μm . (E to G) Construction of NAND gate by coupling phototransduction with a catalytic cascade. Transmembrane signaling system containing sucrose was interfaced with Inv (input A) and GOx (input B), where the presence of both inputs [i.e., (1,1) for input] converted sucrose into gluconic acid, causing a pH decrease, which inhibited the phototransduction (0 for output). Otherwise, phototransduction led to amplified fluorescence and the formation of coacervate microdroplets (1 for output). Scale bars, 3 μm . Error bars represent SD of three replications.

To develop a NAND logic gate, we implemented the signaling system containing GVs and sucrose with an enzyme cascade of invertase (Inv, input A) and glucose oxidase (GOx, input B) (Fig. 5, E and F, and fig. S28). The presence of Inv (i.e., 1 for input A) transformed sucrose into fructose and glucose, where the latter was further hydrolyzed by GOx (i.e., 1 for input B) into gluconic acid to lower the solution pH. This input combination [viz., (1,1) for input] resulted in the protonation of imidazole moiety on ImC8, which inhibited the flip-flop translocation of ImC8 and eventually blocked transmembrane signaling (0 for output). By contrast, the presence of combinatorial inputs (0,1), (1,0), or (0,0) resulted in phototransduction and signal amplification (1 for output; Fig. 5, E and F), as well as the formation of coacervate microdroplets inside GVs (Fig. 5G).

Furthermore, we were able to develop an AND logic gate by using 450-nm light (input A) and adenine (input B) as two inputs in the copper ion-containing signal transduction system (fig. S29). Following light irradiation (input A), the activated messenger (i.e., ImC8) was subsequently coordinated with copper ions, leading to the blockage of signaling pathway (0 for output). The presence of adenine (input B), a competing ligand with a higher binding affinity ($\log K = 8.4$) toward copper, outcompeted copper-imidazole coordination ($\log K = 4.3$) and thereby reactivated the signaling pathway. This system was thus described as an AND logic gate, where the activity (viz., fluorescence increase, 1 for output) was observed only in the presence of both inputs (light and adenine). Using the same computing protocol, we developed a cascade logic gate by coupling the photoreceptor-mediated signaling with urease-catalyzed hydrolysis of urea (figs. S30 and S31).

DISCUSSION

In summary, we constructed an artificial phototransduction system capable of harvesting light, converting photon energy into chemical information, and transmitting and amplifying the signal, which ultimately activates downstream targets and drives LLPS, a mechanism underlying the formation of membraneless organelles. Key to our design is the development of amphiphilic ruthenium-bipyridine complexes as membrane-anchored photoreceptors, which specifically located at the outer leaf of the artificial membranes, selectively sensed the light illumination in the wavelength range of 400 to 515 nm to efficiently secrete a catalytic messenger. The wavelength selectivity of light harvesting enables the photoreceptors to capture informational cues of blue light from sunlight. Unlike GPCRs that transmit extracellular signals through conformational changes of integral receptors, in this work, the photoactivated messenger occurring on the outer leaf of membrane was transferred to the inner side of artificial cells via a process of flip-flop translocation, a typical movement of passive diffusion. The chemical signal of translocated messenger was further transduced through a hydrolysis reaction to generate a messenger with fluorescent signals and initiate complex coacervation through LLPS. Notably, the messenger (alkyl imidazole) acted as an artificial enzyme to generate the chemical signal, which was also distinguished from cellular signaling transductions (55). The chemical structures of messengers and the membrane fluidity play a central role in affecting diffusive transport rate of messengers, which subsequently regulated the photoreceptor-mediated signaling. The length of lipid acyl chains, the presence of unsaturated bonds, the lipid composition, and environmental temperature strongly affected the efficiency of phototransduction, which can be quantitatively predicted from T_m and GP of lipid membranes. Our synthetic photoreceptors allowed for converting extracellular photon signals into intracellular responses including the formation of artificial organelles and protocellular subcompartmentalization. We further explored the physiochemical factors (e.g., pH, metal ions, biomolecules, and enzymes) to regulate photoreceptor-mediated signaling cascades and integrated chemical signal networks and biological interactions into the development of different Boolean logic gates.

Together, this work offers a strategy to construct a synthetic cellular system with biomimetic functions; however, it is still far from real life. The phototransduction cascade includes light harvesting to activate imidazole, flip-flop motion of messenger (alkyl imidazole), and messenger-catalyzed hydrolysis of a fluorogenic substrate. Photoactivation of imidazole was completed within 3 min (Fig. 1C), while the other steps were less efficient, which eventually led to a slow signaling rate. This issue can be addressed by selecting an artificial enzyme with a higher activity or conducting transmembrane signaling at a higher temperature to accelerate the reaction. Alternatively, photoactivation of a bioactive messenger (e.g., an enzyme effector or inhibitor) that can traffic into cytoplasm will allow us to efficiently stimulate (proto)cellular responses. Because the phototransduction is regulated by membrane fluidity, our construct can be further developed as a tool to interrogate molecular diffusion (e.g., flip-flop) on lipid membranes and to study the membrane properties in response to external stimuli. This will help us to understand the biological process and signaling occurring on the lipid bilayer. Compared to biological signaling, the artificial system is less satisfying because photo cycles of photoreceptor are not enabled. A

different mechanism involving a reversible photophysical or photochemical process will be a solution to this problem. We envision that this flexible synthetic platform can be further used to interface with complex metabolic reaction networks for cell-cell communications in multicellular systems and embodied protocell computation.

MATERIALS AND METHODS

Materials

1-Bromooctane, 1-bromodecane, 1-bromododecane, 1,2-epoxydecane, imidazole, sodium 8-hydroxypyrene-1,3,6-trisulfonate, and dichlorobis(2,2'-bipyridine)ruthenium(II) dihydrate were obtained from Bidepharm. Inv (≥ 200 U/mg) from baker's yeast (*Saccharomyces cerevisiae*) was purchased from MREDA. DEAE-dextran and lipase were obtained from Macklin. GOx (*Aspergillus niger*, 100 to 250 U/mg, 150 kDa) was obtained from Shanghai Yuanye Bio-Technology Co., Ltd. Urease, and FITC and FITC-dextran were from Sigma-Aldrich. All lipids, including DPPC, DMPC, POPC, and cholesterol were purchased from Aladdin. Polycarbonate membrane (200 nm) and mini-extruder kits were purchased from Avanti Polar Lipids. The other chemicals were commercially available and used without further purification.

Synthesis of ImC8, ImC10, ImC10', and ImC12

Alkyl imidazoles were synthesized using the method as shown in Fig. S1. Typically, a round-bottom flask was charged with bromide (1.0 eq.), imidazole (1.1 eq.), and potassium carbonate (1.6 eq.) in *N,N'*-dimethylformamide. The mixture was stirred at 150°C overnight. Organic solvent was removed under vacuum and the crude product was purified on a silica gel column, eluted with ethyl acetate. Solvent removal yielded product as a light yellow oil or white powder. The purity of products was verified with ^1H NMR (400 MHz, CDCl_3). δ (ImC8): 7.48 (s, 1H), 7.07 (s, 1H), 6.92 (s, 1H), 3.94 (t, $J = 7.2$ Hz, 2H), 1.79 (dd, $J = 13.9, 7.0$ Hz, 2H), 1.29 (d, $J = 10.5$ Hz, 10H), and 0.89 (t, $J = 6.8$ Hz, 3H). δ (ImC10): 7.48 (s, 1H), 7.07 (s, 1H), 6.92 (s, 1H), 3.94 (t, $J = 7.2$ Hz, 2H), 1.79 (dd, $J = 14.0, 7.1$ Hz, 2H), 1.47 to 1.19 (m, 14H), and 0.90 (t, $J = 6.8$ Hz, 3H). δ (ImC10'): 7.47 (s, 1H), 7.03 (d, $J = 9.9$ Hz, 1H), 6.95 (s, 1H), 6.20 (s, 1H), 4.00 (t, $J = 6.9$ Hz, 2H), 3.26 (q, $J = 6.5$ Hz, 2H), 2.22 to 2.11 (m, 2H), 2.00 (p, $J = 6.8$ Hz, 2H), 1.63 (dd, $J = 14.9, 7.6$ Hz, 2H), 1.59 to 1.02 (m, 4H), and 0.89 (t, $J = 6.9$ Hz, 3H). δ (ImC12): 7.48 (s, 1H), 7.07 (s, 1H), 6.92 (s, 1H), 3.94 (t, $J = 7.2$ Hz, 2H), 1.83 to 1.69 (m, 2H), 1.44 to 1.21 (m, 18H), and 0.90 (t, $J = 6.8$ Hz, 3H).

Synthesis of ImC8-OH

A round-bottom flask was charged with 1.18 g (17.3 mmol) of imidazole and 2.0 g (15.6 mmol) of 1,2-epoxyoctane in 20 ml of isopropanol. The mixture was reacted at 50°C overnight and the solvent was removed under vacuum. The product was purified on a silica gel column, eluted with dichloromethane (DCM)/MeOH (10:1). Solvent removal yielded ImC8-OH as a light yellow oil. ^1H NMR (400 MHz, CDCl_3) δ : 7.37 (s, 1H), 6.91 (d, $J = 4.2$ Hz, 2H), 3.97 (q, $J = 6.5$ Hz, 1H), 3.92 to 3.74 (m, 2H), 1.81 to 1.18 (m, 10H), and 0.89 (q, $J = 6.6$ Hz, 3H).

HPLC analysis of photodegradation of photoreceptors

The photocleavage of photoreceptors was performed on reversed-phase HPLC (Shimadzu) using water/acetonitrile (0.1%

trifluoroacetic acid) as the mobile phase on a C18 column (4.6 mm by 250 mm, 5- μ m particle size). The ratio of organic phase was increased from 5 to 95% within 60 min.

Preparation of LUVs

Substrate-loaded unilamellar vesicles were prepared by the thin-film hydration/extrusion method. (i) Typically, a desired amount of the lipid solution in DCM was added to a glass vial and dried under a stream of nitrogen (N_2). The residual solvent was then removed under vacuum. The dried lipid film containing 2 mg of lipid was then rehydrated in 1 ml of 2 mM PrPTS in phosphate solution (10 mM, pH 7) and vortexed for 30 s. The resulting solution was extruded 29 times through a polycarbonate membrane with 200-nm pores (nucleopore). The untrapped PrPTS was removed from the LUV suspension by size exclusion chromatography through a Sephadex G-50 column. The LUV solution was diluted to lipid concentration (1 mg/ml), stored in the dark, and used within 12 hours. POPC, POPC/cholesterol, and DMPC LUVs were prepared using the same protocol. (ii) DPPC LUVs were prepared following the above protocol except that hydration and extrusion process was conducted at 50°C (above T_m) and 5% of 1, 2-distearoyl-*sn*-glycero-3-phosphoethanolamine-poly(ethylene glycol) was added to stabilize LUVs from aggregation.

Dynamic light scattering

Dynamic light scattering measurements of the as-prepared LUVs were performed on a Malvern Zetasizer Nano ZS (Malvern). Each sample was repeated three times.

Cryo-transmission electron microscopy

Cryo-transmission electron microscopy (TEM) samples of LUVs were prepared in a controlled environment vitrification system. To prepare TEM samples, a small drop of solution was placed on a 300-mesh copper grid, and a thin film was produced by blotting off the redundant liquid with a piece of filter paper. The copper grid was then quickly dipped into liquid ethane cooled by liquid nitrogen. The vitrified samples were then stored in liquid nitrogen before transferring to a cryogenic sample holder (Gatan 626) and examined by a JEM-2200FS transmission electron microscope (200 kV) at -174°C .

Fluorescence recovery after photobleaching

FRAP experiments were conducted on a Nikon A1RSi with a $\times 100$ oil immersion lens. For coacervate droplets encapsulated in GVs, circular regions of interest were bleached with a 488-nm laser for 2 s, and subsequent fluorescence recovery of the bleached area was recorded. The FRAP recovery curve was averaged from three experiments.

Preparation of GVs

The GVs were prepared from gel-assisted lipid hydration method as reported previously. Briefly, dry poly(vinyl alcohol) (PVA) films were prepared by first spreading a 10 weight % (wt %) PVA aqueous solution on precleaned glass vial, followed by drying at 50°C for 0.5 hours. On each of the dry PVA films, a 5- μ l drop of a POPC stock solution (2 mg of phospholipid dissolved in DCM) was then cast and dried under vacuum overnight. Last, the lipid films were hydrated in a solution containing PrPTS or PrPTS/DEAE-dextran to yield GVs. The as-prepared GVs were centrifuged at 5000 rpm, and the supernatant was discarded to remove the

untrapped substrates and polycation. The purification was repeated until no substrate was detected in the supernatant. The resulted GV pellet was redispersed in buffer solution and stored in the dark.

Determination of GP of lipid membranes

GP was measured on a fluorometer using Laurdan as a probe. To vesicles solutions, a stock solution of Laurdan (2.5 μ M) in ethanol was added and the mixture was incubated in the dark overnight. The fluorescence emission was measured on a fluorometer (excitation wavelength, 350 nm; emission wavelength, 435 and 500 nm). The value of GP was determined from the following formula

$$\text{GP} = \frac{I_{435} - I_{500}}{I_{435} + I_{500}}$$

where I_{435} and I_{500} were the fluorescence intensity at 435 and 500 nm, respectively.

FRET analysis to determine the location of photoreceptor on membrane

To localize photoreceptors on the lipid membrane, we performed distance-dependent FRET using HPTS and Rec-1 as energy acceptor and donor, respectively. (i) To validate the FRET in solution, a mixture containing 5 μ M HPTS and 120 μ M Rec-1 was prepared. The fluorescence spectrum from HPTS/Rec-1 and HPTS was then recorded, and the fluorescence quenching of HPTS by Rec-1 confirmed the FRET between HPTS (energy donor) and Rec-1 (energy acceptor). (ii) In second experiment, POPC GVs loaded with HPTS (2 mM) in the inner aqueous phase were prepared from the hydrogel-assisted hydration method as described above. Rec-1 (0.12 mM) was then added to the vesicular solution, and the mixture was incubated at room temperature over a period of 10 min, allowing for the insertion of Rec-1 into lipid membrane. The fluorescence spectrum from HPTS/GVs was then recorded, and the fluorescence quenching was analyzed. (iii) In another experiment, POPC GVs were prepared from the hydrogel-assisted hydration method as described above. Rec-1 was then added to the vesicular solution, and the mixture was incubated at room temperature over a period of 10 min, allowing for the insertion of Rec-1 into lipid membrane. HPTS was added to the POPC/Rec-1 vesicular solution, and the fluorescence spectrum from HPTS/GVs was then recorded.

Catalytic activity of ImC8

The catalytic activity of ImC8 was tested using PrPTS and pNPA as the fluorogenic and chromogenic substrate, respectively. (i) Typically, ImC8 (0.25 mM) was dissolved in phosphate buffer (10 mM, pH 7.0), and a freshly prepared solution of PrPTS was added to reach a concentration of 0.25 mM. Immediately, the fluorescence intensity of the solution was measured on a fluorometer at room temperature over a period of 5 min, with the 480-nm excitation and 520-nm emission. (ii) Similarly, ImC8 was dissolved in phosphate buffer (10 mM, pH 7.0), and a freshly prepared solution of pNPA in methanol was added to reach a concentration of 0.5 mM. The absorbance at 400 nm was measured immediately on an ultraviolet-visible (UV-vis) spectrometer over a period of 10 min.

Catalytic activity of photoreceptor after photoactivation

The catalytic activity of photoreceptor (Rec-1) was tested using PrPTS and pNPA as the fluorogenic and chromogenic substrate, respectively. (i) Typically, Rec-1 (0.1 mM) was dissolved in phosphate

buffer (10 mM, pH 7.0), and a freshly prepared solution of PrPTS was added to reach a concentration of 0.5 mM. Immediately after photoactivation with a 450-nm light-emitting diode (LED) lamp, the fluorescence intensity of the solution was measured on a fluorometer at room temperature over a period of 60 min, with the 480-nm excitation and 520-nm emission. (ii) Similarly, Rec-1 was dissolved in phosphate buffer (10 mM, pH 7.0), and a freshly prepared solution of pNPA in acetonitrile was added to reach a concentration of 0.5 mM. Immediately, the UV-vis absorbance at 400 nm was measured on a UV-vis spectrometer at room temperature over a period of 5 min.

Phototransduction on POPC GVs

Typically, POPC GVs (2 mg/ml) containing fluorogenic substrate PrPTS (2 mM) were prepared with the gel-assisted rehydration method as described above. To this mixture, 0.12 mM photoreceptor was added and incubated at room temperature in the dark for 10 min. Upon irradiation with a 450-nm LED lamp for 5 min, time-dependent flow cytometry was obtained on a Novo Cyte 2060R flow cytometer. Confocal laser scanning microscopy (CLSM) measurements of GVs were carried out on a Zeiss LSM 880 microscope using a $\times 63$ oil immersion lens with a diode laser (405 nm for PrPTS excitation), an argon laser (488 nm for HPTS excitation), and a HeNe laser (543 nm for Nile red excitation).

Phototransduction on POPC LUVs

Typically, 200-nm POPC LUVs containing fluorogenic substrate PrPTS (2 mM) were prepared with the hydration/extrusion method as described above. To this mixture, 40 μ M photoreceptor was added and incubated at room temperature in the dark for 10 min. Upon irradiation with a 450-nm LED lamp for 5 min, the fluorescence intensity at 520 nm was monitored for 60 min on a plate reader.

Leakage test of fluorogenic substrate (PrPTS)

To confirm that PrPTS did not diffuse out of the membrane, we compared the performance of histidine and alkyl imidazole (the messenger molecule) toward catalytic hydrolysis of PrPTS. (i) Typically, 200 μ l of PrPTS solution (40 μ M) in phosphate buffer (10 mM, pH 7.0) was added to a 96-well plate. Histidine or alkyl imidazole (40 μ M) was added. The fluorescence intensity of catalytic product HPTS was recorded for 1 hour on a plate reader. (ii) In another experiment, the fluorogenic substrate PrPTS (2 mM) was encapsulated in POPC vesicles (1 mg/ml) in phosphate buffer (10 mM, pH 7.0). The LUV solution was then added to a 96-well plate, and 40 μ M histidine or alkyl imidazole was added. The fluorescence intensity of catalytic product HPTS was recorded for 1 hour on a plate reader. The excitation and emission wavelength was 480 and 520 nm, respectively.

Phase diagram of DEAE-dextran/HPTS coacervation

To obtain the phase diagram of DEAE-dextran/HPTS, stock solutions of DEAE-dextran and HPTS solutions at varied concentrations were mixed with different ratios. The samples were incubated for ca. 10 min, and their coacervation behaviors were studied with optical microscopy and solution turbidity.

ImC8-triggered DEAE-dextran/PrPTS coacervation via LLPS

To a mixture of DEAE-dextran (5 mg/ml) and PrPTS (3.2 mM) in phosphate buffer (10 mM, pH 7.0), 120 μ M ImC8 was added to

initiate the hydrolysis reaction. The process of catalyzed coacervation was immediately monitored with optical density, fluorescence, microscopy visualization, and flow cytometry.

Transmembrane signaling triggered LLPS within POPC GVs

Typically, POPC GVs (2 mg/ml) containing fluorogenic substrate PrPTS at varied concentrations (0.6, 0.8, 3.2, and 4.6 mM) and polycation DEAE-dextran (1.0, 3.0, 5.0, and 10 mg/ml) were prepared with the gel-assisted rehydration method as described above. To this mixture, a desired amount of photoreceptor was added and incubated at room temperature in the dark for 10 min. Upon irradiation with a 450-nm LED lamp for 5 min, time-dependent flow cytometry was obtained on a Novo Cyte 2060R flow cytometer, and fluorescence intensity from catalytic product HPTS was recorded on fluorometer (Shimadzu LC-16P). CLSM measurements of GVs were carried out on a Zeiss LSM 880 using a $\times 63$ oil immersion lens with a diode laser (405 nm for PrPTS excitation), an argon laser (488 nm for HPTS excitation), and a HeNe laser (543 nm for Nile red excitation).

Effect of metal ions on transmembrane signaling

GVs were prepared with the hydrogel-assisted rehydration method. Typically, 180 μ l of PVA (10 wt %) was added to a glass vial and dried in vacuum to remove water. Two hundred microliters of POPC solution in DCM (10 mg/ml) was added and streamed with nitrogen to remove the organic solvent. Residual DCM was further removed in vacuum for 20 min. To this lipid film, an aqueous solution (1 ml) containing DEAE-dextran (5 mg/ml) and 3.2 mM PrPTS in HEPES (10 mM, pH 7.0) was added. After hydration for 30 min, the supernatant was transferred to an Eppendorf tube and centrifuged at 5000 rpm for 6 min. After removing the supernatant, the pellet was washed with water four times to remove untrapped substrates. The pellet was redispersed in 1 ml of HEPES buffer (10 mM, pH 7.0) to obtain POPC GVs loaded with DEAE-dextran and PrPTS. To the above solution containing the GVs, Rec-1 (120 μ M) and a series of metal ions (10 mM) were added. After incubation in the dark for 10 min, the fluorescence intensity (480-nm excitation and 520-nm emission) was measured on a plate reader over a period of 60 min.

Effect of solution pH on transmembrane signaling

GVs were prepared with the hydrogel-assisted rehydration method. Typically, 180 μ l of PVA (10 wt %) was added to a glass vial and dried in vacuum to remove water. Two hundred microliters of POPC solution in DCM (10 mg/ml) was added and streamed with nitrogen to remove the organic solvent. Residual DCM was further removed in vacuum for 20 min. To this lipid film, an aqueous solution (1 ml) containing DEAE-dextran (5 mg/ml) and 3.2 mM PrPTS in phosphate buffer (10 mM, pH 7.0) was added. After hydration for 30 min, the supernatant was transferred to an Eppendorf tube and centrifuged at 5000 rpm for 6 min. After removing the supernatant, the pellet was washed with water four times to remove untrapped substrates. The pellet was redispersed in 1 ml of phosphate buffer (10 mM; pH 6.0, 7.0, and 8.0) to obtain POPC GVs loaded with DEAE-dextran and PrPTS. To the above solution containing the GVs, 120 μ M Rec-1 was added and the solution was incubated for 10 min in the dark. Then, the fluorescence intensity (480-nm excitation and 520-nm emission) was measured on a plate reader over a period of 60 min.

Construction of NAND logic gates with GVs

GVs were prepared with the hydrogel-assisted rehydration method. Typically, 180 μl of PVA (10 wt %) was added to a glass vial and dried in vacuum to remove water. Two hundred microliters of POPC solution in DCM (10 mg/ml) was added and streamed with nitrogen to remove the organic solvent. Residual DCM was further removed in vacuum for 20 min. To this lipid film, an aqueous solution (1 ml) containing DEAE-dextran (5 mg/ml) and 3.2 mM PrPTS in phosphate buffer (10 mM, pH 7.0) was added. After hydration for 30 min, the supernatant was transferred to an Eppendorf tube and centrifuged at 5000 rpm for 6 min. After removing the supernatant, the pellet was washed with water four times to remove untrapped substrates. The pellet was redispersed in 1 ml of phosphate buffer (10 mM, pH 7.0) to obtain POPC GVs loaded with DEAE-dextran and PrPTS. To the above solution containing the GVs, 120 μM Rec-1 and 25 mM sucrose were added and incubated for 10 min in the dark. Then, Inv (0.06 mg/ml, input A) and GOx (0.14 mg/ml, input B) were used as two input signals. For all cases, the samples were incubated in the dark for 1.0 hours and irradiated with 450-nm light for 5 min. The fluorescence intensity was measured on a plate reader after 1-hour incubation. Then, the fluorescence intensity (480-nm excitation and 520-nm emission) was measured on a plate reader, and the formation of coacervate droplets was recorded on a fluorescence microscope.

Construction of NOR logic gates with GVs

GVs were prepared with the hydrogel-assisted rehydration method. Typically, 180 μl of PVA (10 wt %) was added to a glass vial and dried in vacuum to remove water. Two hundred microliters of POPC solution in DCM (10 mg/ml) was added and streamed with nitrogen to remove the organic solvent. Residual DCM was further removed in vacuum for 20 min. To this mixture, an aqueous solution (1 ml) containing DEAE-dextran (5 mg/ml) and 3.2 mM PrPTS in HEPES buffer (10 mM, pH 7.0) was added and hydrated for 30 min. The supernatant was transferred to an Eppendorf tube and centrifuged at 5000 rpm for 6 min. The supernatant was discarded and the pellet was washed with water four times to completely remove untrapped substrates. The pellet was dispersed in 1 ml of HEPES buffer (10 mM, pH 7.0) to obtain POPC GVs loaded with DEAE-dextran and PrPTS. To a solution containing the above GVs, 120 μM Rec-1 was added and incubated for 10 min in the dark. After that, Cu^{2+} (1.0 mM, input A) and HCl (final pH 6, input B) were used as two input signals. The samples were irradiated with 450-nm light for 5 min and incubated at room temperature for 1 hour. Then, the fluorescence intensity (480-nm excitation and 520-nm emission) was measured on a plate reader, and the formation of coacervate droplets was recorded on a fluorescence microscope.

Construction of AND logic gates with GVs

GVs were prepared with the hydrogel-assisted rehydration method. Typically, 180 μl of PVA (10 wt %) was added to a glass vial and dried in vacuum to remove water. Two hundred microliters of POPC solution in DCM (10 mg/ml) was added and streamed with nitrogen to remove the organic solvent. Residual DCM was further removed in vacuum for 20 min. To this mixture, an aqueous solution (1 ml) containing DEAE-dextran (5 mg/ml) and 3.2 mM PrPTS in HEPES buffer (10 mM, pH 7.0) was added and hydrated for 30 min. The supernatant was transferred to an

Eppendorf tube and centrifuged at 5000 rpm for 6 min. The supernatant was discarded and the pellet was washed with water four times to remove untrapped substrates. The pellet was dispersed in 1 ml of HEPES buffer (10 mM, pH 7.0) to obtain POPC GVs loaded with DEAE-dextran and PrPTS. To a solution containing the above GVs in a 96-well plate, 120 μM Rec-1 and 1 mM Cu^{2+} were added and the mixture was incubated for 10 min in the dark. Subsequently, 5 mM adenine (input A) and 450-nm light irradiation for 5 min (input B) were used as two input signals. After incubation for 1 hour, the fluorescence intensity (480-nm excitation and 520-nm emission) was measured on a plate reader, and the formation of coacervate droplets was recorded on a fluorescence microscope.

Urease-mediated hydrolysis of urea to regulate solution pH

Typically, urease (2 mg/ml) was dissolved in phosphate buffer (10 mM, pH 6.0), and a solution of urea (40 mM) was added to initiate the urease-mediated hydrolysis reaction of urea. The solution pH was recorded every 30 s on a pH meter (AQUASEARCH-ER AB33PH).

Inv- and GOx-mediated pH changes

In detail, Inv (0.06 mg/ml) and GOx (0.14 mg/ml) were dissolved in phosphate buffer (10 mM, pH 7.0). A solution of sucrose (25 mM) was added to the mixture to initiate the cascade enzymatic reaction. Solution pH was recorded over a period of 70 min at room temperature.

Supplementary Materials

This PDF file includes:

Supplementary Materials and Methods
Figs. S1 to S31
References

REFERENCES AND NOTES

- B. C. Buddingh', J. Elzinga, J. C. M. van Hest, Intercellular communication between artificial cells by allosteric amplification of a molecular signal. *Nat. Commun.* **11**, 1652 (2020).
- J. W. Hindley, D. G. Zheleva, Y. Elani, K. Charalambous, L. M. C. Barter, P. J. Booth, C. L. Bevan, R. V. Law, O. Ces, Building a synthetic mechanosensitive signaling pathway in compartmentalized artificial cells. *Proc. Natl. Acad. Sci. U.S.A.* **116**, 16711–16716 (2019).
- A. Joesaar, S. Yang, B. Bögels, A. van der Linden, P. Pieters, B. V. V. S. P. Kumar, N. Dalchau, A. Phillips, S. Mann, T. F. A. de Greef, DNA-based communication in populations of synthetic protocells. *Nat. Nanotechnol.* **14**, 369–378 (2019).
- W. Mu, Z. Ji, M. Zhou, J. Wu, Y. Lin, Y. Qiao, Membrane-confined liquid-liquid phase separation toward artificial organelles. *Sci. Adv.* **7**, eabf9000 (2021).
- C. E. G. Hoskin, V. R. Schild, J. Vinals, H. Bayley, Parallel transmission in a synthetic nerve. *Nat. Chem.* **14**, 650–657 (2022).
- Q. Li, S. Li, X. Zhang, W. Xu, X. Han, Programmed magnetic manipulation of vesicles into spatially coded prototissue architectures arrays. *Nat. Commun.* **11**, 232 (2020).
- R. Lentini, S. P. Santero, F. Chizzolini, D. Cecchi, J. Fontana, M. Marchiorotto, C. Del Bianco, J. L. Terrell, A. C. Spencer, L. Martini, M. Forlin, M. Assfalg, M. Dalla Serra, W. E. Bentley, S. S. Mansy, Integrating artificial with natural cells to translate chemical messages that direct *E. coli* behaviour. *Nat. Commun.* **5**, 4012 (2014).
- V. Mukwaya, S. Mann, H. Dou, Chemical communication at the synthetic cell/living cell interface. *Commun. Chem.* **4**, 161 (2021).
- Y. Lyu, R. Peng, H. Liu, H. Kuai, L. Mo, D. Han, J. Li, W. Tan, Protocells programmed through artificial reaction networks. *Chem. Sci.* **11**, 631–642 (2020).
- R. Saha, S. Verbanic, I. A. Chen, Lipid vesicles chaperone an encapsulated RNA aptamer. *Nat. Commun.* **9**, 2313 (2018).
- K. A. Podolsky, N. K. Devaraj, Synthesis of lipid membranes for artificial cells. *Nat. Rev. Chem.* **5**, 676–694 (2021).

12. M. S. Long, A.-S. Cans, C. D. Keating, Budding and asymmetric protein microcompartmentation in giant vesicles containing two aqueous phases. *J. Am. Chem. Soc.* **130**, 756–762 (2008).
13. K. Kurihara, M. Tamura, K.-i. Shohda, T. Toyota, K. Suzuki, T. Sugawara, Self-reproduction of supramolecular giant vesicles combined with the amplification of encapsulated DNA. *Nat. Chem.* **3**, 775–781 (2011).
14. W. Zong, S. Ma, X. Zhang, X. Wang, Q. Li, X. Han, A fissionable artificial eukaryote-like cell model. *J. Am. Chem. Soc.* **139**, 9955–9960 (2017).
15. S. Deshpande, F. Brandenburg, A. Lau, M. G. F. Last, W. K. Spoelstra, L. Reese, S. Wunnavu, M. Dogterom, C. Dekker, Spatiotemporal control of coacervate formation within liposomes. *Nat. Commun.* **10**, 1800 (2019).
16. C. Love, J. Steinkühler, D. T. Gonzales, N. Yandrapalli, T. Robinson, R. Dimova, T.-Y. D. Tang, Reversible pH-responsive coacervate formation in lipid vesicles activates dormant enzymatic reactions. *Angew. Chem. Int. Ed. Engl.* **59**, 5950–5957 (2020).
17. Y. Dreher, K. Jahnke, E. Bobkova, J. P. Spatz, K. Göpfrich, Division and regrowth of phase-separated giant unilamellar vesicles. *Angew. Chem. Int. Ed.* **60**, 10661–10669 (2021).
18. M. Weiss, J. P. Frohnmayer, L. T. Benk, B. Haller, J.-W. Janiesch, T. Heitkamp, M. Börsch, R. B. Lira, R. Dimova, R. Lipowsky, E. Bodenschatz, J.-C. Baret, T. Vidakovic-Koch, K. Sundmacher, I. Platzman, J. P. Spatz, Sequential bottom-up assembly of mechanically stabilized synthetic cells by microfluidics. *Nat. Mater.* **17**, 89–96 (2018).
19. I. A. Chen, R. W. Roberts, J. W. Szostak, The emergence of competition between model protocells. *Science* **305**, 1474–1476 (2004).
20. A. E. Engelhart, K. P. Adamala, J. W. Szostak, A simple physical mechanism enables homeostasis in primitive cells. *Nat. Chem.* **8**, 448–453 (2016).
21. M. Marguet, C. Bonduelle, S. Lecommandoux, Multicompartmentalized polymeric systems: towards biomimetic cellular structure and function. *Chem. Soc. Rev.* **42**, 512–529 (2013).
22. C. Martino, S.-H. Kim, L. Horsfall, A. Abbaspourad, S. J. Rosser, J. Cooper, D. A. Weitz, Protein expression, aggregation, and triggered release from polymersomes as artificial cell-like structures. *Angew. Chem. Int. Ed.* **51**, 6416–6420 (2012).
23. B. Stadler, A. D. Price, R. Chandrawati, L. Hosta-Rigau, A. N. Zelikin, F. Caruso, Polymer hydrogel capsules: En route toward synthetic cellular systems. *Nanoscale* **1**, 68–73 (2009).
24. R. J. R. W. Peters, M. Marguet, S. Marais, M. W. Fraaije, J. C. M. van Hest, S. Lecommandoux, Cascade reactions in multicompartmentalized polymersomes. *Angew. Chem. Int. Ed.* **53**, 146–150 (2014).
25. M. Li, R. L. Harbron, J. V. M. Weaver, B. P. Binks, S. Mann, Electrostatically gated membrane permeability in inorganic protocells. *Nat. Chem.* **5**, 529–536 (2013).
26. X. Huang, M. Li, D. C. Green, D. S. Williams, A. J. Patil, S. Mann, Interfacial assembly of protein-polymer nano-conjugates into stimulus-responsive biomimetic protocells. *Nat. Commun.* **4**, 2239 (2013).
27. X. Wang, X. Liu, X. Huang, Bioinspired protein-based assembling: Toward advanced life-like behaviors. *Adv. Mater.* **32**, 2001436 (2020).
28. A. Dupin, F. C. Simmel, Signalling and differentiation in emulsion-based multi-compartmentalized in vitro gene circuits. *Nat. Chem.* **11**, 32–39 (2019).
29. P. Gobbo, A. J. Patil, M. Li, R. Harniman, W. H. Briscoe, S. Mann, Programmed assembly of synthetic protocells into thermoresponsive prototissues. *Nat. Mater.* **17**, 1145–1153 (2018).
30. G. Bolognesi, M. S. Friddin, A. Salehi-Reyhani, N. E. Barlow, N. J. Brooks, O. Ces, Y. Elani, Sculpting and fusing biomimetic vesicle networks using optical tweezers. *Nat. Commun.* **9**, 1882 (2018).
31. R. Merindol, S. Loescher, A. Samanta, A. Walther, Pathway-controlled formation of meso-structured all-DNA colloids and superstructures. *Nat. Nanotechnol.* **13**, 730–738 (2018).
32. L. Tian, N. Martin, P. G. Bassindale, A. J. Patil, M. Li, A. Barnes, B. W. Drinkwater, S. Mann, Spontaneous assembly of chemically encoded two-dimensional coacervate droplet arrays by acoustic wave patterning. *Nat. Commun.* **7**, 13068 (2016).
33. M. J. Booth, V. R. Schild, A. D. Graham, S. N. Olof, H. Bayley, Light-activated communication in synthetic tissues. *Sci. Adv.* **2**, e160005 (2016).
34. O. Adir, M. R. Albalak, R. Abel, L. E. Weiss, G. Chen, A. Gruber, O. Stauer, Y. Kurman, I. Kaminer, J. Shklover, J. Shainsky-Roitman, I. Platzman, L. Gepstein, Y. Shechtman, B. A. Horwitz, A. Schroeder, Synthetic cells with self-activating optogenetic proteins communicate with natural cells. *Nat. Commun.* **13**, 2328 (2022).
35. T. Chakraborty, S. M. Bartelt, J. Steinkühler, R. Dimova, S. V. Wegner, Light controlled cell-to-cell adhesion and chemical communication in minimal synthetic cells. *Chem. Commun.* **55**, 9448–9451 (2019).
36. A. F. Mason, B. C. Buddingh, D. S. Williams, J. C. M. van Hest, Hierarchical self-assembly of a copolymer-stabilized coacervate protocell. *J. Am. Chem. Soc.* **139**, 17309–17312 (2017).
37. T.-Y. D. Tang, C. R. C. Hak, A. J. Thompson, M. K. Kuimova, D. S. Williams, A. W. Perriman, S. Mann, Fatty acid membrane assembly on coacervate microdroplets as a step towards a hybrid protocell model. *Nat. Chem.* **6**, 527–533 (2014).
38. S. Liu, Y. Zhang, M. Li, L. Xiong, Z. Zhang, X. Yang, X. He, K. Wang, J. Liu, S. Mann, Enzyme-mediated nitric oxide production in vasoactive erythrocyte membrane-enclosed coacervate protocells. *Nat. Chem.* **12**, 1165–1173 (2020).
39. Y. Elani, R. V. Law, O. Ces, Vesicle-based artificial cells as chemical microreactors with spatially segregated reaction pathways. *Nat. Commun.* **5**, 5305 (2014).
40. X. Liu, Y. Xiong, C. Zhang, R. Lai, H. Liu, R. Peng, T. Fu, Q. Liu, X. Fang, S. Mann, W. Tan, G-quadruplex-induced liquid-liquid phase separation in biomimetic protocells. *J. Am. Chem. Soc.* **143**, 11036–11043 (2021).
41. S. Yang, A. Joesaar, B. W. A. Bogels, S. Mann, T. F. A. de Greef, Protocellular CRISPR/Cas-based diffusible communication using transcriptional RNA signaling. *Angew. Chem. Int. Ed.* **134**, e2022024 (2022).
42. M. Karin, Signal transduction from cell surface to nucleus in development and disease. *FASEB J.* **6**, 2581–2590 (1992).
43. M. J. Langton, F. Keymeulen, M. Giaccia, N. H. Williams, C. A. Hunter, Controlled membrane translocation provides a mechanism for signal transduction and amplification. *Nat. Chem.* **9**, 426–430 (2017).
44. M. J. Langton, N. H. Williams, C. A. Hunter, Recognition-controlled membrane translocation for signal transduction across lipid bilayers. *J. Am. Chem. Soc.* **139**, 6461–6466 (2017).
45. M. De Poli, W. Zawodny, O. Quinoner, M. Lorch, S. J. Webb, J. Clayden, Conformational photoswitching of a synthetic peptide foldamer bound within a phospholipid bilayer. *Science* **352**, 575–580 (2016).
46. F. G. A. Lister, B. A. F. Le Bailly, S. J. Webb, J. Clayden, Ligand-modulated conformational switching in a fully synthetic membrane-bound receptor. *Nat. Chem.* **9**, 420–425 (2017).
47. K. Bernitzki, T. Schrader, Entirely artificial signal transduction with a primary messenger. *Angew. Chem. Int. Ed.* **48**, 8001–8005 (2009).
48. J. Hou, X. Jiang, F. Yang, L. Wang, T. Yan, S. Liu, J. Xu, C. Hou, Q. Luo, J. Liu, Supramolecularly regulated artificial transmembrane signal transduction for 'ON/OFF'-switchable enzyme catalysis. *Chem. Commun.* **58**, 5725–5728 (2022).
49. H. Chen, L. Zhou, C. Li, X. He, J. Huang, X. Yang, H. Shi, K. Wang, J. Liu, Controlled dimerization of artificial membrane receptors for transmembrane signal transduction. *Chem. Sci.* **12**, 8224–8230 (2021).
50. K. Y. Lee, S.-J. Park, K. A. Lee, S.-H. Kim, H. Kim, Y. Meroz, L. Mahadevan, K.-H. Jung, T. K. Ahn, K. K. Parker, K. Shin, Photosynthetic artificial organelles sustain and control ATP-dependent reactions in a protocellular system. *Nat. Biotechnol.* **36**, 530–535 (2018).
51. S. Theis, A. Iturriandi, C. Gorsche, M. Orthofer, M. Lunzer, S. Baudis, A. Ovsiyanikov, R. Liska, U. Monkowius, I. Teasdale, Metallo-supramolecular gels that are photocleavable with visible and near-infrared irradiation. *Angew. Chem. Int. Ed.* **56**, 15857–15860 (2017).
52. A. Aguzzi, M. Altmeyer, Phase separation: Linking cellular compartmentalization to disease. *Trends Cell Biol.* **26**, 547–558 (2016).
53. K. K. Nakashima, M. H. I. van Haren, A. A. M. Andre, I. Robu, E. Spruijt, Active coacervate droplets are protocells that grow and resist Ostwald ripening. *Nat. Commun.* **12**, 3819 (2021).
54. L. E. Kipinos, B. Song, H. Sigel, Metal ion-coordinating properties of imidazole and derivatives in aqueous solution: Interrelation between complex stability and ligand basicity. *Inorg. Chim. Acta* **280**, 50–56 (1998).
55. V. Y. Arshavsky, T. D. Lamb, E. N. Pugh, Jr, G proteins and phototransduction. *Annu. Rev. Physiol.* **64**, 153–187 (2002).
56. D. S. Daniels, E. J. Petersson, J. X. Qiu, A. Schepartz, High-resolution structure of a β -peptide bundle. *J. Am. Chem. Soc.* **129**, 1532–1533 (2007).

Acknowledgments

Funding: This work was financially supported by the National Natural Science Foundation of China (grant nos. 22172007, 52221006, and 22072159) and the Fundamental Research Funds for the Central Universities (buctrc202015 and PT2208). **Author contributions:** Conceptualization: H.L. and Y.L. Methodology: H.L., Y.Q., and Y.L. Investigation: H.L., Y.Y., J.C., K.S., C.S., Y.J., and L.J. Visualization: H.L., Y.Q., and Y.L. Supervision: J.L., Y.Q., and Y.L. Writing—original draft: H.L., Y.Q., and Y.L. Writing—review and editing: H.L., Y.Q., and Y.L. All authors discussed the results and have given approval to the final version of the manuscript. **Competing interests:** The authors declare that they have no competing interests. **Data and materials availability:** All data needed to evaluate the conclusions in the paper are present in the paper and/or the Supplementary Materials.

Submitted 25 August 2022

Accepted 27 January 2023

Published 1 March 2023

10.1126/sciadv.ade5853